JOURNAL OF MATERIALS SCIENCE 31 (1996) 4007–4016

Plasma-chemical synthesis of ultradispersed iron oxides with pigment qualification

G. P. VISSOKOV, P. S. PIRGOV
Institute of Electronics, Bulgarian Academy of Sciences, 72 Tsarigradsko Shaussee blvd., Sofia 1784, Bulgaria

The conditions are investigated for preparing ultradispersed iron oxides with pigment qualification (iron oxide pigments) via oxidation in electric arc low temperature plasma (LTP) of: iron dichloride (crystal hydrate), iron sulfate (monohydrate), roughly dispersed iron and burnt pyrites. Using a simplified one-dimensional model, calculations are made describing the motion, heating, melting and evaporation of iron particles of <50 μm size; these agree well with experimental results. A procedure is proposed for formation of ultradispersed particle (UDP) structures. Depending on the plasma-chemical process (PCP) parameters, one can control the specific surface (dispersity) of the pigments. The influence is studied of aluminium and aluminium oxide additives on the pigmental properties of iron oxides. Depending on the PCP conditions and the UDP dispersity, the pigment's colour varies from black through dark brown, red-brown, red-violet to light brown. The pigment possesses high surface coverage combined with medium oil absorption and good compatibility with other pigments.

1. Introduction

The techniques currently used for preparation of iron oxides with pigment qualification consist of oxidation of iron sulfate [1–7], iron di- and trichloride [1, 4, 8–12], elemental iron [13], iron carbonate [1], etc.

Preparation of iron oxide pigments using plasma techniques is a new trend in the field of plasma chemistry. In the USA, a method was patented for obtaining calcium, magnesium, aluminium, lead, titanium, chromium and iron oxides by means of oxidation of the respective chlorides under LTP conditions [14]. A method has also been described [15] for production of finely dispersed iron oxides through oxidation of $FeCl_2$ by an oxygen-containing gas in chlorine plasma. The product obtained has a particle size of 100–200 nm. Pure ferric oxide (Fe_2O_3) and magnetite powder (Fe_3O_4) were blown into a plasma jet [16]. When Fe_3O_4 was used as a raw material, the solid content formed in a nitrogen plasma jet included about 40% FeO.

Due to the scant patent data [14, 15], the authors' task has been to investigate the possibilities of preparing highly dispersed, respectively, ultradispersed, iron oxides with pigment qualification from iron dichloride (crystal hydrate, $FeCl_2 \cdot (3–4)H_2O$), iron sulfate (monohydrate, $FeSO_4 \cdot H_2O$), elemental iron and pyrites burnt using oxidation in an electric arc LTP, and, further, to establish the optimal process parameters. Thermodynamic calculations were first carried out in order to determine the value of Gibbs' energy and the equilibrium constant of the reaction

$$2Fe + O_2 = 2FeO \quad (1)$$

The results of the calculations are given in Table I; one can see that the oxidation process should be performed at temperatures not exceeding 3500 K.

In what concerns reaction kinetics, the limiting role is widely accepted in heterogeneous plasma chemical processes of the stage of condensed-phase evaporation. The important consequence follows that, besides creating suitable thermodynamic conditions (temperature and reagents ratio), one must also ensure sufficient residence time of the particles in the plasma-chemical reactor (PCR), so that they can evaporate completely. Guaranteeing these conditions allows one to synthesize the desired products in the gaseous phase. After an appropriate fast cooling of the reacting mixture, i.e. at a defined rate of quenching, $dT/d\tau$ (where T is the temperature and τ the time) the product is obtained in the desired dispersed form. Bearing in mind the properties of dispersed materials, one believes that the following classification is justified

1. ultradispersed (including clusters), 1–50 nm;
2. highly dispersed (finely dispersed), 50–500 nm;
3. micrometre size powders, 0.5–100 μm; and
4. roughly dispersed, above 0.1 mm.

The above considerations make obvious the necessity of modelling the particle evaporation process. As a result, one can obtain sufficiently accurate data to determine the optimal process parameters, namely, the PCR size, the particle residence time in the reactor, the temperature profile along the reactor axis, the temperature near the wall, the temperature of the PCR wall, etc. Theoretical and experimental studies of the

0022–2461

TABLE I Temperature dependencies of Gibbs' energy ($\Delta G_T \times 10^{-3}$) and equilibrium constant according to Equation 1

Temperature (K)	1800	2000	3000	4000	6000
Gibbs' energy (kJ mol^{-1} K^{-1})	−40.17	−34.81	−28.17	23.87	97.70
Equilibrium constant (mol s^{-1})	7.76×10^4	6.45×10^3	1.12×10^2	4.90×10^{-2}	2.75×10^{-4}

process are hindered by the short duration and the non-steady state and non-equilibrium character of the accompanying phenomena, as well as by the multiple determining factors and their complex interdependence. Making use of an approach for modelling the particle evaporation process in electric arc LTP, published earlier [17], a set of eight differential equations [17, 18] were solved for the plasma velocity, the particle velocity, the rate of particle temperature variation before and after melting, the particle melting time, the rate of particle diameter variation before and after boiling, and the gas temperature, while accounting for the vapour heating and the heat transfer to the PCR walls. Since among the raw materials used iron has the highest boiling temperature (T_b = 3023 K), a set of equations was solved for iron particles with radii of 5 and 15 μm and a flow rate of 3.3×10^{-5} kg s^{-1}, with Ar as a plasma forming gas (flow rate of 7.92×10^{-4} kg s^{-1}) and N_2 as a powder carrier gas (flow rate of 1.35×10^{-4} kg s^{-1}). The initial plasma temperature is 8000 K. As Fig. 1 shows, iron particles with diameters below 30 μm evaporate completely in the PCR. The data obtained concerning particle temperature, particle melting and evaporation time and the gas temperature as functions of the time of contact between the gas and the particles, and that between the gas and the PCR walls, are in good agreement with experimental results. The set of equations used [17, 18] enables one to select the optimal parameters (PCR size, the minimal time needed for contact between the plasma jet and the particle, place of introducing the quenching reagents, heat resistance of the PCR building materials, etc.). In order to simplify the calculations and, above all, to reduce the number of physicochemical quantities involved (for some of which high temperature reference data are lacking), the following assumptions were made: the powder was monodispersive, the temperature gradient along the particle radius was zero, mixing was instantaneous and homogeneous, gas flow around the particle was continuous, the chemical reactions and the condensation did not affect the gas temperature, and the gas temperature was constant across the PCR cross-section; the equations for particle plasma heat exchange, for particle motion and for the radiative losses were then solved jointly as follows

1. The thermal energy variation, dQ, for a spherical particle for a time, $d\tau$, due to heat exchange with the plasma is

$$dQ = \alpha_T \Delta T F \, d\tau \tag{2}$$

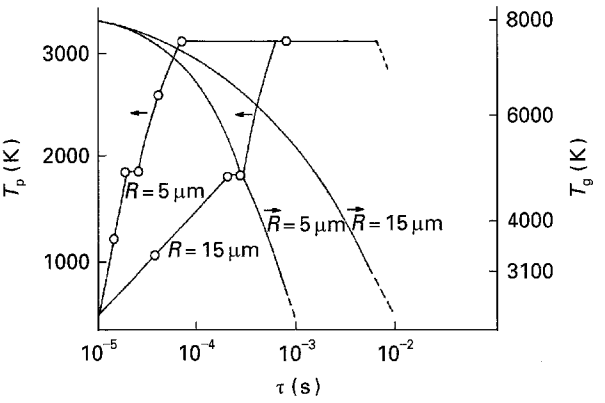

Figure 1 Variation of the temperature of the iron particles (T_p) and of the gas (T_g) as functions of the time for contact (τ) and the particle radius (R).

where

$$\alpha_T = \mathrm{Nu}\frac{\lambda_g}{d_p}; \quad F = \pi d_p^2;$$

$$\Delta T = \langle T_g \rangle - \langle T_p \rangle; \quad \langle T_p \rangle = \tfrac{1}{2}(T_i + T_{i+1})$$

Nu is the Nusselt number; λ, heat conductivity; d, diameter; F, particle surface; and subscripts g and p refer to the gas and particle, respectively. Angled brackets refer to the mean values.

2. The particle thermal energy variation during a phase transition, e.g. solid–liquid or liquid–vapour transition, is

$$dQ = G_p c_p \Delta T_p \quad (T_p \neq \text{const}) \tag{3}$$

$$dQ = G_p \Delta L_p \quad (T_p = \text{const}) \tag{4}$$

where

$$G_p = \frac{\pi d_p^3}{6}\rho_p; \quad \Delta T_p = T_{i+1} - T_i$$

G_p is the current particle weight; c_p, the specific heat of the particle; L_p, the particle melting heat; and ρ, the density.

3. The joint solution of Equations 2 and 3 yields an equation describing the particle plasma heat exchange; when the radiative losses are then accounted for using the Stefan–Boltzmann equation

$$dQ = \sigma T^4 \tag{5}$$

where $\sigma = 5.778 \times 10^{-8}$ J m^{-2} s^{-1} K^{-4}, one obtains the particle temperature variation with time

$$\frac{dT_p}{d\tau} = \frac{3\mathrm{Nu}\lambda_g(T_g - T_p)}{d_p^2 c_p \rho_p} - \frac{6\sigma T^4}{\pi d_p^3 c_p \rho_p} \tag{6}$$

Combining Equations 2 and 4, one finds the particle melting time, τ_b

$$d\tau_b = \frac{d_p^2 \rho_p L_p}{6\mathrm{Nu}\lambda_g(T_g - T_p)} + \frac{\sigma T^4}{\mathrm{Nu}\lambda_g d_p(T_g - T_p)} \quad (7)$$

4. The particle diameter variation due to evaporation is found by solving Equations 2 and 4 for $L_p = L_{pv}$, where the latter is the particle evaporation heat, and by taking the radiative losses into account

$$\frac{dd_p}{d\tau} = \frac{\mathrm{Nu}\lambda_g(T_p - T_g)}{d_p \rho_p L_{pv}} + \frac{\sigma T^4}{\pi d_p^2 \rho_p L_{pv}} \quad (8)$$

5. The acceleration, V_p, of the spherical particle in the gas flow is

$$G_p \frac{dV_p}{d\tau} = \frac{1}{2} C_D F(V_g - V_p)^2 \quad (9)$$

where C_D is the drag coefficient.

For Re values in the one to ten range, usually reached in plasma chemical equipment $C_D = [24f(\mathrm{Re})/\mathrm{Re}]$, and Equation 9 can be written as

$$\frac{dV_p}{d\tau} = \frac{18f(\mathrm{Re})}{\mathrm{Re}\, d_p \rho_p}(V_g - V_p)$$

or

$$\frac{dV_p}{d\tau} = \frac{18\mu_g f(\mathrm{Re})}{\rho_g d_p^2}(V_g - V_p) \quad (10)$$

where μ_g is the dynamic viscosity of the gas.

6. The mean velocity of the plasma jet is determined by integrating the gas velocity across the PCR cross-section

$$\langle V \rangle = \int_0^{V_g} V_g \, dF \quad (11)$$

Calculations were carried out for the case of evaporation of iron particles with radii of 5, 10, 15, 20, 25 and 30 μm. Fig. 2 presents the particle temperature variation as a function of its initial radius and location along the PCR axis, while Fig. 3 shows particle radius variation as a function of the same variables.

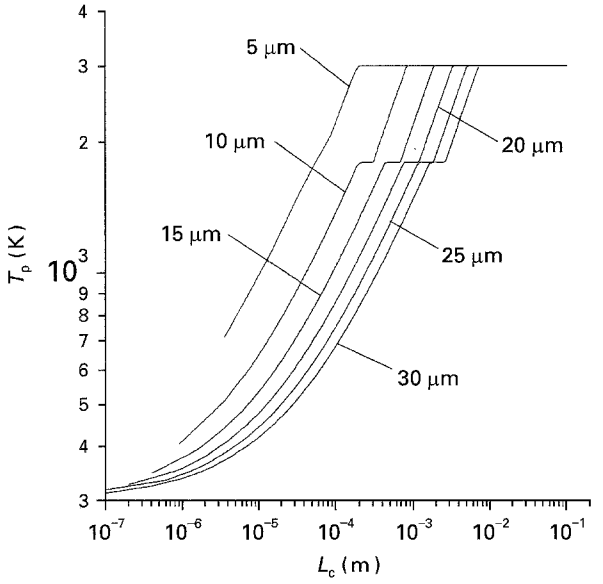

Figure 2 Variation of the temperature of the iron particles (T_p) as a function of their location along the PCR axis (L_c).

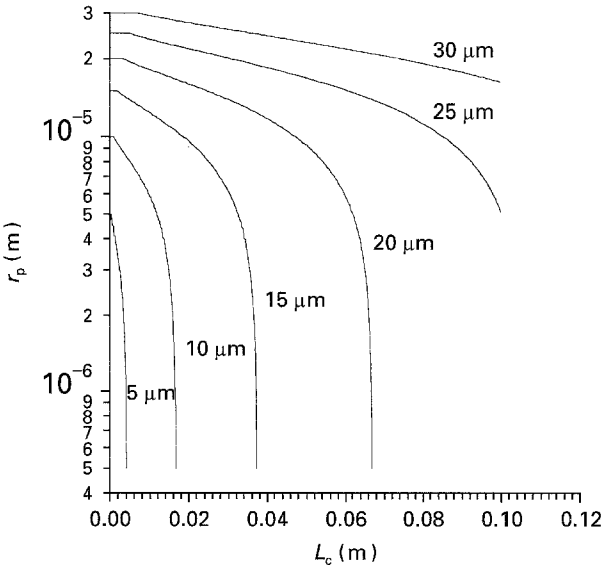

Figure 3 Variation of the radius of the iron particles (r_p) as a function of their location along the PCR axis (L_c).

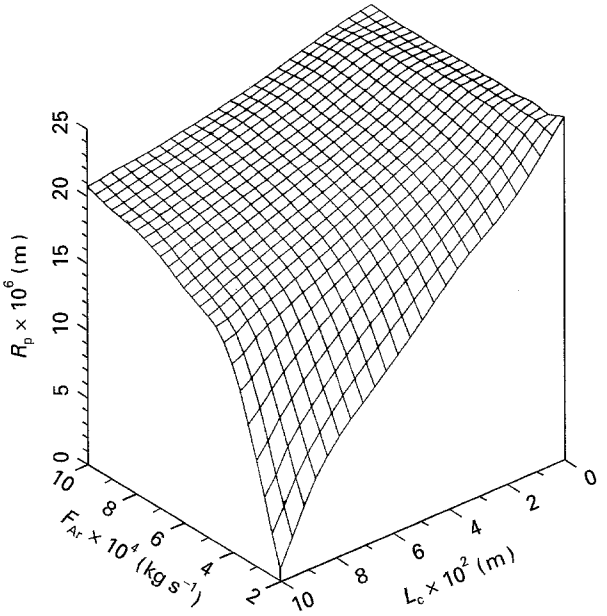

Figure 4 Variation of the radius of an iron particle (R_p) with a diameter of 50 μm as a function of the flow rate of the plasma forming Ar gas (F_{Ar}) and of the location along the PCR axis (L_c).

Figs 4 and 5 illustrate the least favourable case, namely, decreasing iron particle radius due to evaporation, for a maximum initial radius of 50 μm, as a function of the flow rate of the plasma-forming Ar and of its location along the PCR axis (the PCR length is set at 100 mm). It is seen that at the PCR output the iron particle has evaporated down to a radius of about 1 μm (Fig. 4), while the particle evaporates completely when a temperature of 8000 K is reached (Fig. 5).

2. Experimental procedure

The investigation was carried out using the equipment schematically shown in Fig. 6. It consists of a CW electric arc plasmatron using Ar as the plasma-forming gas at a flow rate of 2000 l h^{-1}, a PCR, a quenching device, a powder trapping chamber, a vibration

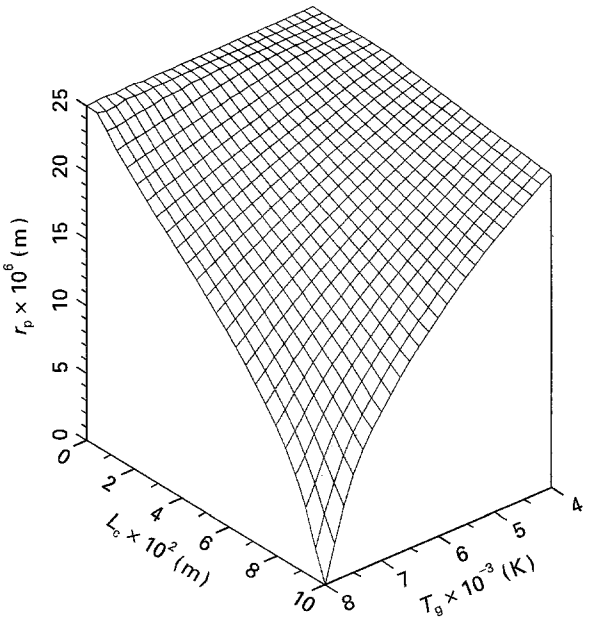

Figure 5 Variation of the radius of an iron particle (r_p) with initial diameter of 50 μm as a function of the plasma-jet temperature (T_g) and of the location along the PCR axis (L_c).

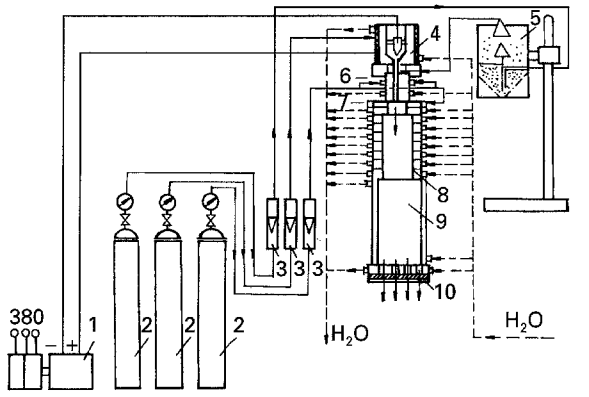

Figure 6 Schematic diagram of the plasma-chemical apparatus for preparation of iron oxide pigments: (1) power supply and rectifier; (2) bottles with plasma forming, powder carrying and quenching gases; (3) flow rate meters; (4) electric arc plasmatron, $D_c = 5$ mm; (5) vibration powder feeder; (6) water-cooled PCR; (7) gas-quenching of the reaction products; (8) quenching device; (9) powder trapping chamber; and (10) filter.

powder feeder, and cooling water and reagents feeding systems. The electric power consumed by the plasmatron is controlled by varying the supply current between 100 and 600 A. The average temperature of the plasma and the PCR is measured calorimetrically. Quenching is achieved on the cool walls of the powder trapping chamber. The raw materials are fed after the arc active region, and oxygen is used as the powder carrying gas in the vibration feeder at two flow rates: 380 and 760 $l\,h^{-1}$. The iron oxide pigments fabricated are characterized by their specific surface (determined using the Kliyatchko–Gurvitch method [19]), chemical composition (X-ray analysis, determining the Fe_2O_3, Fe_3O_4, respectively Fe^{3+}/Fe^{2+}, and $FeO \cdot Al_2O_3$ content), bulk mass, colour, surface coverage, oil absorption and dispersity (electron microscopy).

Three series of experiments were performed on $FeCl_2 \cdot (3–4)H_2O$ (specific surface, $S = 2\ m^2\,g^{-1}$) oxidation in the electric arc LTP, namely: oxidation without additives (Table II); oxidation in the presence of 15 mass % aluminium (Table III); and oxidation in the presence of 5 mass % Al_2O_3 (Table IV). For each series the results are presented for two operating modes determined by the flow rate of the oxidizing and powder carrying gas (oxygen): 380 and 760 $l\,h^{-1}$. The experimental results of oxidation in electric arc LTP of $FeSO_4 \cdot H_2O$ ($S = 1\ m^2\,g^{-1}$, Table V), elemental iron ($S = 7\ m^2\,g^{-1}$, Table VI), elemental iron in the presence of 5 mass % Al_2O_3 (Table VII) and burnt pyrites ($S = 9\ m^2\,g^{-1}$, Table VIII) exhibit quantitative and qualitative dependencies as in the case of $FeCl_2 \cdot (3–4)H_2O$ oxidation under the same conditions.

3. Results and discussion

As the experimental results presented (Tables II–IV) on $FeCl_2 \cdot (3–4)H_2O$ oxidation in electric arc LTP demonstrate, the specific surface of the iron oxides mixture obtained passes through a maximum as the average temperature in the PCR increases (Fig. 7). When the plasmatron power is raised (the temperature is increased), the specific surface grows [ultradispersed particles (UDP) are formed] due to the fact that at high PCR temperatures chemical reactions take place in the gaseous phase (Equation 1) and the time for condensation after quenching is insufficient for UDP growth. In fact, this is confirmed by the scheme adopted for UDP structure formation (Fig. 8). When the

TABLE II Some technological parameters of the $FeCl_2 \cdot (3–4)H_2O$ oxidation process and composition of the ultradispersed pigment

No.	Power (kW)	Plasma temperature (K)	Reactor temperature (K)	O_2 ($l\,h^{-1}$)	Specific surface ($m^2\,g^{-1}$)	Fe_2O_3 (mass %)	Fe_3O_4 (mass %)	Fe^{3+}/Fe^{2+}
1	5.4	3700	1400	380	5	16.6	83.4	2.6
2	8.4	5450	1930	380	10	40.3	59.7	4.0
3	11.6	7400	2500	380	17	53.0	47.0	5.3
4	15.0	9400	3150	380	17	53.1	46.9	5.3
5	19.8	12000	4000	380	16	69.8	30.2	8.8
6	5.6	3800	1350	760	12	23.3	76.7	2.9
7	8.4	5450	1650	760	19	47.5	52.5	4.7
8	11.6	7800	2500	760	15	49.3	50.7	4.9
9	15.0	9400	2950	760	15	70.2	29.8	9.1
10	18.0	11250	3450	760	6	75.5	24.5	11.2

TABLE III Some technological parameters of $FeCl_2 \cdot (3-4)H_2O$ with 15 wt% Al oxidation process and composition of the ultradispersed pigment

No.	Power (kW)	Plasma temperature (K)	Reactor temperature (K)	O_2 ($l\,h^{-1}$)	Specific surface ($m^2\,g^{-1}$)	Fe_2O_3 (mass %)	Fe_3O_4 (mass %)	$FeO \cdot Al_2O_3$ (mass %)	Fe^{3+}/Fe^{2+}
1	2.7	2100	900	380	55	29.0	49.9	21.1	2.5
2	3.4	2500	1050	380	63	30.9	41.3	27.8	2.4
3	5.4	3700	1400	380	59	30.9	44.5	24.6	2.5
4	7.5	4950	1750	380	81	23.6	61.4	15.0	2.5
5	8.1	5600	1900	380	84	23.8	61.7	14.5	2.5
6	11.2	7150	2450	380	85	17.1	69.6	13.3	2.3
7	15.5	9700	3200	380	63	16.3	68.0	15.7	2.1
8	2.7	2100	900	760	78	27.4	49.1	23.6	2.3
9	5.2	2550	1000	760	89	26.8	50.2	23.0	2.3
10	8.1	5300	1750	760	87	14.4	66.5	19.1	2.0
11	11.2	7150	2300	760	90	19.5	55.3	25.2	2.0
12	15.5	9700	3000	760	93	19.3	55.8	24.9	2.0

TABLE IV Some technological parameters of $FeCl_2 \cdot (3-4)H_2O$ and 5 wt% Al_2O_3 oxidation process and composition of the ultradispersed pigment

No.	Power (kW)	Plasma temperature (K)	Reactor temperature (K)	O_2 ($l\,h^{-1}$)	Specific surface ($m^2\,g^{-1}$)	Fe_2O_3 (mass %)	Fe_3O_4 (mass %)	Al_2O_3 (mass %)	Fe^{3+}/Fe^{2+}
1	5.2	3550	1350	380	21	37.6	60.6	1.8	3.8
2	8.1	5600	1900	380	22	37.2	59.2	3.6	3.8
3	10.8	6900	2350	380	25	42.4	55.5	2.1	4.2
4	14.0	8800	2950	380	27	59.8	37.0	3.2	6.8
5	4.8	3350	1200	760	32	41.3	56.1	2.6	4.1
6	7.8	5100	1750	760	37	68.0	29.5	2.5	8.8
7	10.8	6900	2200	760	37	66.8	30.2	3.0	8.6
8	14.0	8800	2750	760	37	78.1	17.5	4.4	15.4

TABLE V Some technological parameters of the $FeSO_4 \cdot (3-4)H_2O$ oxidation process and composition of the ultradispersed pigment

No.	Power (kW)	Plasma temperature (K)	Reactor temperature (K)	O_2 ($l\,h^{-1}$)	Specific surface ($m^2\,g^{-1}$)	Fe_2O_3 (mass %)	Fe_3O_4 (mass %)	Fe^{3+}/Fe^{2+}
1	5.2	3550	1350	380	12	12.5	87.5	2.4
2	8.4	5450	1930	380	15	45.3	54.7	4.5
3	11.6	7400	2500	380	23	52.0	48.0	5.3
4	14.5	9100	2850	380	15	58.2	41.8	6.2
5	17.4	10850	3300	380	18	64.1	35.9	7.3
6	5.8	3900	1400	760	13	38.8	61.2	3.9
7	8.7	5650	1900	760	19	56.4	43.6	5.9
8	11.6	7400	2400	760	29	63.0	37.0	7.1
9	14.0	8800	2750	760	21	55.4	44.6	5.7
10	17.4	10900	3350	760	15	64.6	35.4	7.4

TABLE VI Some technological parameters of Fe oxidation process (O_2 flow 380 $l\,h^{-1}$) and composition of the ultradispersed pigment

No.	Power (kW)	Plasma temperature (K)	Reactor temperature (K)	Specific surface ($m^2\,g^{-1}$)	Fe_2O_3 (mass %)	Fe_3O_4 (mass %)	Fe^{3+}/Fe^{2+}
1	5.2	3550	1350	24	30.7	69.3	3.3
2	8.1	5600	1900	24	43.3	56.7	4.3
3	11.2	7150	2450	21	37.5	62.5	3.8
4	12.5	7900	2700	43	54.3	45.7	5.6
5	15.6	9750	3250	33	58.6	41.4	6.2

TABLE VII Some technological parameters of the Fe with 5 wt % Al_2O_3 oxidation process and composition of the ultradispersed pigment

No.	Power (kW)	Plasma temperature (K)	Reactor temperature (K)	O_2 ($l\,h^{-1}$)	Specific surface ($m^2\,g^{-1}$)	Fe_2O_3 (mass %)	Fe_3O_4 (mass %)	Fe^{3+}/Fe^{2+}
1	5.0	3450	1300	380	26	11.2	84.2	2.4
2	7.8	5100	1800	380	24	37.1	58.8	3.9
3	10.8	6900	2350	380	25	43.4	50.5	4.6
4	14.0	8800	2950	380	24	13.1	82.0	2.5
5	5.8	3900	1400	760	26	19.5	77.3	2.8
6	8.1	5300	1750	760	29	34.3	63.4	3.7
7	11.2	7150	2300	760	27	26.9	69.2	3.2
8	14.0	8800	2750	760	15	32.8	60.6	3.6

TABLE VIII Some technological parameters of burnt pyrites waste oxidation process (O_2 flow $760\,l\,h^{-1}$) and composition of the ultradispersed pigment

No.	Power (kW)	Plasma temperature (K)	Reactor temperature (K)	Specific surface ($m^2\,g^{-1}$)	Fe_2O_3 (mass %)	Fe_3O_4 (mass %)	Fe^{3+}/Fe^{2+}
1	5.6	3800	1350	11	–	–	–
2	9.3	6000	1950	26	56.7	35.4	6.6
3	15.2	9550	3000	39	60.6	32.7	7.4
4	17.5	10950	3350	13	71.0	21.9	11.4

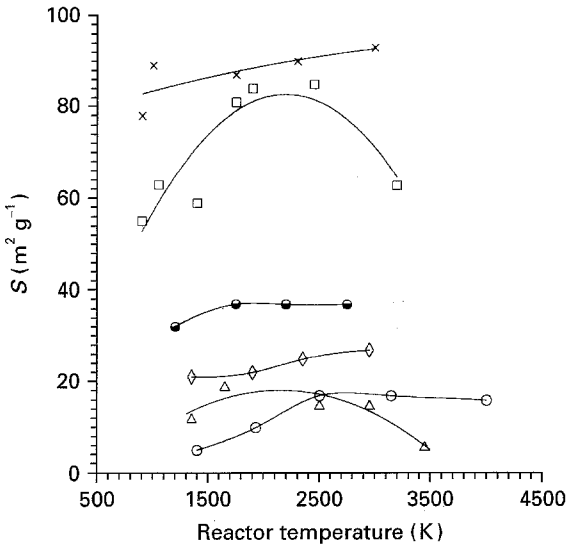

Figure 7 Dependence of the specific surface (S) on the average temperature in the PCR (T): (○ and △) oxidation of $FeCl_2 \cdot (3–4)H_2O$; (□ and ×) in the presence of 15 mass % Al; (◇ and ◒) in the presence of 5 mass % (Al_2O_3 + 3 mass % TiO_2). Oxygen flow rate: (○, □ and ◇) $380\,l\,h^{-1}$, (△, × and ◒) $760\,l\,h^{-1}$.

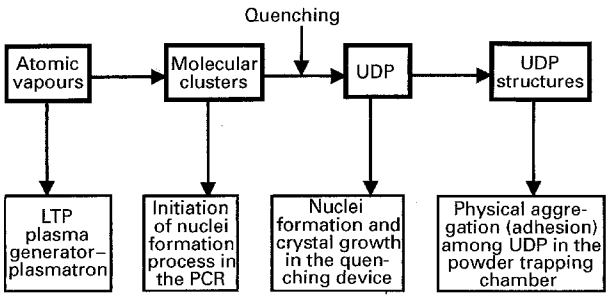

Figure 8 Scheme of formation of UDP structures.

temperature is raised further, the processes of agglomeration and sintering of the existing UDP accelerate so that the specific surface drops (Fig. 7). With all other conditions kept the same, the specific surface rises with the oxygen flow rate due to stabilization of the gas-dynamic operating regime of the PCR.

It was reported earlier [1, 13] that adding 5 mass % aluminium or an aluminium salt affects favourably the properties of iron oxide pigments. The experiments show (Table III) an almost five-fold increase of the specific surface when oxidation takes place in the presence of 15 mass % aluminium, as compared with that of pigments obtained by $FeCl_2$ oxidation without additives. The sharp rise of the specific surface is a result of the inhibiting effect aluminium powder has on end product agglomeration and sintering. This is explained by the fact that the oxidation process leads to the formation of $FeO \cdot Al_2O_3$ spinel (Table III) whose thermal stability is greater than that of the iron oxides.

Adding 5 mass % Al_2O_3 to the initial material also results in an increase of the end product's specific surface, albeit to a lesser degree compared with adding elemental aluminium, probably because of the smaller amount of additive.

X-ray analysis of oxidation products indicates that for $FeCl_2$ oxidation without additives the UDP are composed of two oxides: magnetite (Fe_3O_4) and hematite (Fe_2O_3) (Fig. 9). In addition, the products of the second series (Table III) contain 13–28 mass % spinel ($FeO \cdot Al_2O_3$), while those of the third series comprise insignificant amounts (2–4 mass %) of Al_2O_3 (Table IV).

The Fe^{3+}/Fe^{2+} ratio is indicative of the character of the processes occurring in the plasma jet (Fig. 10). The diversity of these processes and the specific

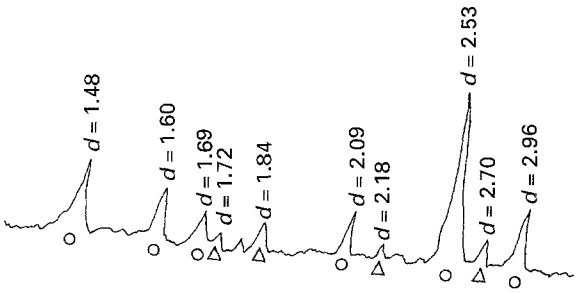

Figure 9 X-ray pattern of an iron oxide pigment, Table II, sample No. 6: (○) Fe_3O_4, (△) Fe_2O_3.

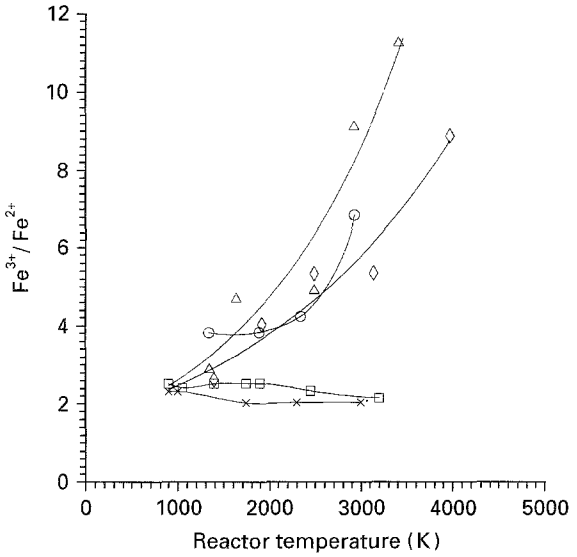

Figure 10 Dependence of the Fe^{3+}/Fe^{2+} in the pigments on the average temperature (T) in the PCR: (○ and ◇) oxidation of $FeCl_2 \cdot (3–4)H_2O$; (□ and ×) in the presence of 15 mass % Al; (△) in the presence of 5 mass % (Al_2O_3 + 3 mass % TiO_2). Oxygen flow rate: (○, □ and △) 380 l h^{-1}; (◇ and ×) 760 l h^{-1}.

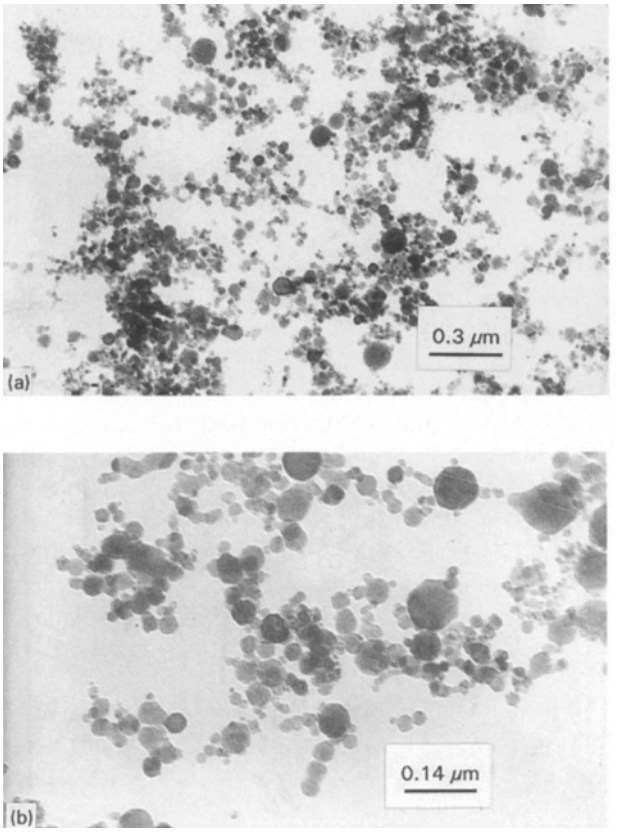

Figure 11 Electron microscope photographs of plasma-chemically synthesized iron oxide pigments: (a) sample No. 12, Table III, magnification × 36 000, 1 mm = 28 nm, (b) sample No. 12, Table III, magnification × 75 000, 1 mm = 11 nm.

conditions in the LTP make interpretation of the experimental results a complicated task. The medium being strongly oxidizing, the entire complex of physical, chemical and thermal processes is dominated by oxidation. Due to stoichiometric excess of oxygen (ten-fold for the first series, twenty-fold for the second), $FeCl_2$ is initially oxidized to Fe_2O_3

$$2FeCl_2 + 1.5O_2 = Fe_2O_3 + 2Cl_2 \quad (12)$$

At temperatures above 1300 K, this reaction is accompanied by the process of hematite disproportioning to magnetite

$$3Fe_2O_3 = 2Fe_3O_4 + 0.5O_2 \quad (13)$$

A complete evaluation of the process in its entirety can be made by accounting for the thermodynamic characteristics of the two reactions (oxidation and thermal decomposition) at the respective temperatures. The reaction rates are enormous, while the time for contact (in this specific PCR $\tau_c = 10^{-4}$ s) is sufficient for thermodynamic equilibrium to be established at a given temperature. This equilibrium determines the ratio of the two oxides (Fe_2O_3 and Fe_3O_4) in the reaction products. At a constant flow rate of the plasma-forming and oxidizing gas, the plasma temperature is a function of the power. Thus, an unequivocal relation becomes obvious between the temperature (or the power consumed by the plasmatron) and the chemical content of the pigments, with all other conditions kept equal.

The results presented (Tables II–IV) allow one to conclude that at low powers (5–10 kW), respectively temperatures, the oxidizing process prevails. As the temperature in the PCR increases, its contribution decreases so that thermal decomposition becomes predominant.

When the oxygen flow rate is raised from 380 to 760 l h^{-1}, the Fe_2O_3 content (respectively the Fe^{3+}/Fe^{2+} ratio) increases weakly (Fig. 10). This is a natural consequence of the mass conservation law, as applied to Equations 12 and 13.

Following the oxidation process in the presence of 15 mass % aluminium is also of interest, not only because of the high dispersity (Fig. 11) of the end products, i.e. the high specific surface value, but also because of the presence of a qualitatively new phase, namely the $FeO \cdot Al_2O_3$ spinel, which changes the colour of the pigment. The appearance of this phase is related to the sharp drop of the Fe^{3+}/Fe^{2+} (Fig. 10) ratio resulting from increased Fe_3O_4 content and decreased Fe_2O_3 content in the samples. This ratio varies within a narrow range, 2.0–2.5 (Table III), for the entire temperature interval investigated and decreases insignificantly when the oxidant amount is increased.

Within the 2000–5000 K temperature interval, the degree of dissociation of ferrochloride is 100%. In this case, the problem is treated by following the general relationships of iron oxidation. According to Baikov's principle [20], the step-like character of the process at temperatures above 843 K is described by

$$Fe \rightarrow FeO \rightarrow Fe_3O_4 \rightarrow Fe_2O_3 \qquad (14)$$

Regardless of the direction of the process (oxidation or reduction), the principle postulates that it is impossible to skip any one of the above steps. In the case considered here, part of the FeO formed in the first step combines with aluminium to produce a spinel ($FeO \cdot Al_2O_3$) and is thus removed from the system. This hinders the oxidation process, leading to formation of a higher oxide and explains the comparatively low Fe_2O_3 content in the reaction products.

Adding about 5 mass % aluminum oxide to $FeCl_2$ does not influence significantly the pigment's content. A certain increase in the Fe_2O_3 content is seen (Table IV), which is due to the catalytic effect Al_2O_3 has on $FeCl_2$ oxidation [3, 13].

The pigments of the first and second series have an almost identical colour (red-brown); the pigment becomes lighter as the power is increased. When 15 mass % aluminium is added, the colour changes to yellow-brown and when the temperature is raised the brown shade becomes stronger. The bulk mass of the pigments of the first series is 0.51 $g\,cm^{-3}$; of the second series, 0.28 $g\,cm^{-3}$; and of the third series, 0.41 $g\,cm^{-3}$. The surface coverage of the pigments is 2–2.5 $g\,m^{-2}$ at medium oil absorption; they exhibit good compatibility with other finely dispersed pigments.

Summarizing the experimental results, one should emphasize the following. Oxidation of $FeCl_2 \cdot (3–4)H_2O$ leads to the formation of pigments with specific surface of 19 $m^2\,g^{-1}$ and with a maximum Fe_2O_3 content of up to 75.5 mass %. They are of red-brown colour with bulk mass of 0.51 $g\,cm^{-3}$. Adding 15 mass % aluminium to the initial materials sharply increases the pigment's specific surface to 93 $m^2\,g^{-1}$; the colour changes to yellow-brown, and the bulk mass, to 0.28 $g\,cm^{-3}$. A new phase is formed, namely ($FeO \cdot Al_2O_3$) spinel. Finally, the pigments fabricated by oxidation of $FeCl_2$ in the presence of 5 mass % Al_2O_3 have a specific surface of 37 $m^2\,g^{-1}$; the predominating phase (up to 78%) is Fe_2O_3, and the bulk mass is 0.41 $g\,cm^{-3}$.

Since pulverization of $FeSO_4 \cdot 7H_2O$ is impossible, its dehydration to monohydrate is necessary at 373 K. The material is then fed uniformly into the PCR by the powder feeder. The experimental results prove the possibility of preparing iron oxide pigments by oxidizing $FeSO_4 \cdot H_2O$ in electric arc LTP (Table V). The specific surface of the pigments obtained reaches 29 $m^2\,g^{-1}$ (Fig. 12), while the Fe_2O_3 content is as high as 65 mass % (Fig. 13). The certain increase observed of the specific surface of the products of the second experimental series as compared to the first is due to the improved hydrodynamic conditions in the system as the amount of powder carrying gas is raised, as well as to changes in the related heat and mass exchange processes.

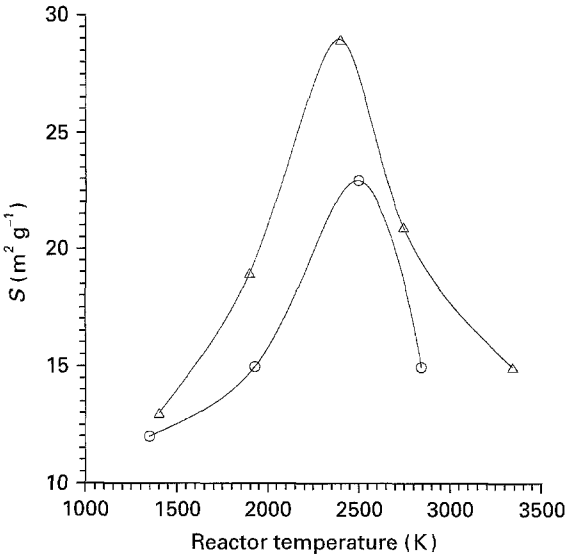

Figure 12 Dependence of the specific surface of the pigments (S) on the average temperature in the PCR (T). Oxygen flow rate: (○) 380 $l\,h^{-1}$, (△) 760 $l\,h^{-1}$.

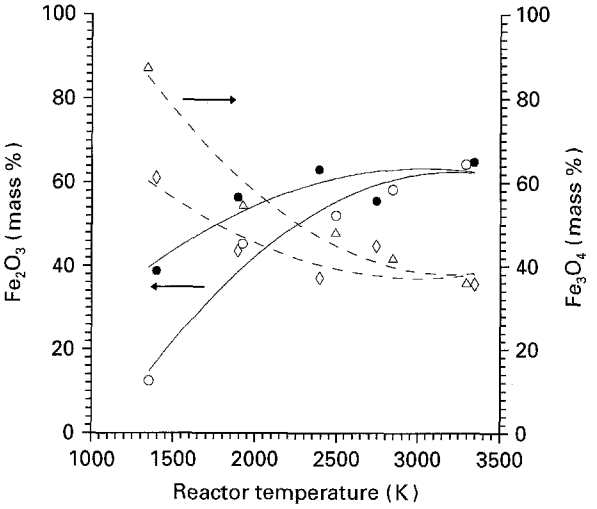

Figure 13 Fe_2O_3 and Fe_3O_4 content in the pigment (mass %) as a function of average temperature in the PCR (T). Oxygen flow rate: (○ and △) 380 $l\,h^{-1}$, (● and ◇) 760 $l\,h^{-1}$.

The X-ray patterns of the products are analogous to those shown in Fig. 9. The salient peaks observed are evidence of the presence in the pigments of only two phases, Fe_3O_4 and Fe_2O_3, both manifested by all their lines. The ratio of the content of the two oxides is a function of power (or the average temperature in the PCR), as the latter is increased, the ratio changes in favour of Fe_2O_3. This trend is revealed more strongly in the first operating mode: from 12.5 to 87.5 mass % in magnetite's favour at a PCR temperature of 1350 K, the ratio shifts from 64.1 to 35.9 mass % in hematite's favour at 3300 K. Obviously, at temperatures exceeding 3300 K, and for an oxygen flow rate of 380 $l\,h^{-1}$, one should expect even higher values of the Fe_2O_3 content in the powders. This, however, will be accompanied on the one hand by a lowering of the specific surface and, consequently, a worsening of the pigment properties of the product, and, on the other, by Gibbs' energy for Equation 1 assuming positive values (or the

equilibrium constant becoming too small). This assumption is supported by the fact that an increase of the PCR temperature from 2500 to 2850 K leads to an increase of the Fe_2O_3 content from 52.0 to 58.2 mass % and, at the same time, to a decrease of the specific surface from 23 to 15 $m^2 g^{-1}$. For each specific case, therefore, one should select the optimal process parameters, bearing in mind the desired properties of the end products (colour, specific surface, etc.).

Fig. 14 presents the Fe^{3+}/Fe^{2+} ratio as a function of the PCR temperature. For an oxidant flow rate of 760 l h^{-1}, the curve passes through a maximum. It is obvious that above a certain PCR temperature the process of thermal Fe_2O_3 decomposition plays a predominant role; as a result, the Fe_3O_4 content increases and, respectively, the Fe^{3+}/Fe^{2+} ratio decreases. At an oxygen flow rate of 380 l h^{-1}, the maximum is weak.

Summing up the experimental results (Table V, Figs 12–14), one should point out that the authors have proved the possibility of obtaining iron oxide pigments by means of oxidizing $FeSO_4 \cdot H_2O$ in electric arc LTP. The specific surface of the pigments produced reaches 29 $m^2 g^{-1}$, with the Fe_2O_3 content approaching 65 mass %. The pigment colour changes from brown at low power (temperatures) to red-brown as the temperature is raised.

Experiments are further reported on oxidizing iron powder with specific surface of 7 $m^2 g^{-1}$, namely, 1.5 g min^{-1} of iron powder is fed into the PCR at an oxygen flow rate of 380 l h^{-1}. The amount of oxidant stoichiometrically needed for this iron consumption, as calculated following the reaction

$$2Fe + 1.5O_2 = Fe_2O_3 \qquad (15)$$

is 27 l h^{-1}, i.e. a fourteen-fold excess of oxygen is ensured.

The aim of the experiment is to clarify the influence of the process parameters and of adding Al_2O_3 on the content and properties of the end products. Thus, two series of experiments are reported: first, oxidation of elemental iron (Table VI) and, second, oxidation of elemental iron in the presence of 5 mass % (Al_2O_3 + 3 mass % TiO_2) (Table VII). When iron powder is used as a raw material (Table VI), the specific surface and the Fe^{3+}/Fe^{2+} ratio pass through a maximum as the average temperature in the PCR is increased, while the pigment's colour changes from dark red-brown to light red-brown to black.

Figs 15 and 16 present X-ray patterns of two pigmented samples obtained by means of elemental iron oxidation in electric arc LTP. For the dark brown sample, one can observe the main peaks of Fe_3O_4 and FeO, and only one Fe_2O_3 peak. A peak of elemental iron is also observed, pointing to the fact that part of the iron has not been oxidized. The colour is, therefore, determined on the one hand by the proportion of black magnetite and brown hematite in the sample, and by the dispersity of the particles on the other. In the presence of only Fe_3O_4 and FeO (Fig. 16) the colour of the pigment is black. A peak of non-oxidized iron is again observed.

As the average temperature in the PCR is raised, the process of thermal decomposition of Fe_2O_3 according

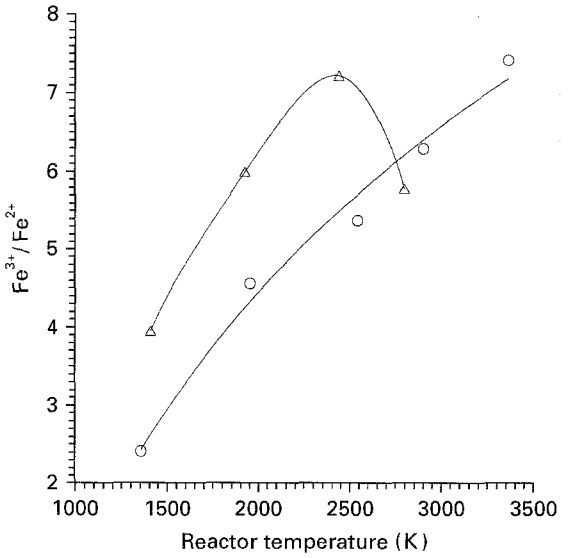

Figure 14 Dependence of the Fe^{3+}/Fe^{2+} ratio on the average temperature in the PCR (T). Oxygen flow rate: (○) 380 l h^{-1}, (△) 760 l h^{-1}.

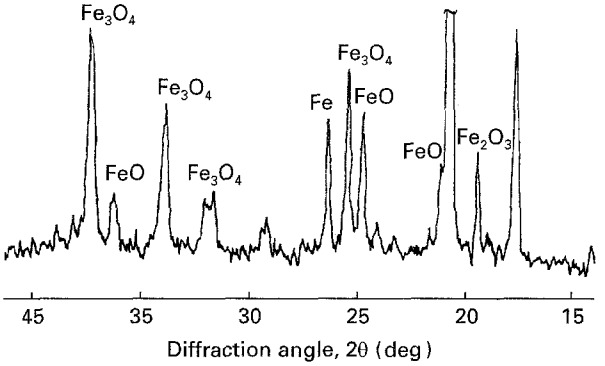

Figure 15 X-ray pattern of iron oxide pigment (dark brown) prepared by oxidation of iron powder in oxygen.

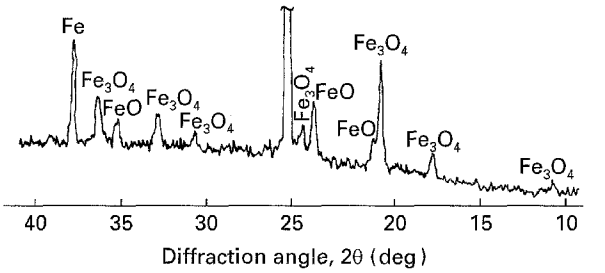

Figure 16 X-ray pattern of iron oxide pigment (black) prepared by oxidation of iron powder in oxygen.

to Equation 13 begins to dominate; as a result, the Fe_3O_4 content in the pigment increases. This is reflected in the pigment's colour; it becomes darker. The average bulk mass is 0.40 g cm^{-3}. Adding 5 mass % (Al_2O_3 + 3 mass % TiO_2) to the initial materials, as well as increasing the flow rate of the powder carrying oxidant, does not affect significantly the pigment's properties.

Table VIII shows the results of heat treatment of burnt pyrites (Fe_2O_3 content 87%) in an electric arc LTP. Fig. 17 illustrates the dependencies of the specific surface on the average temperature in the PCR. At

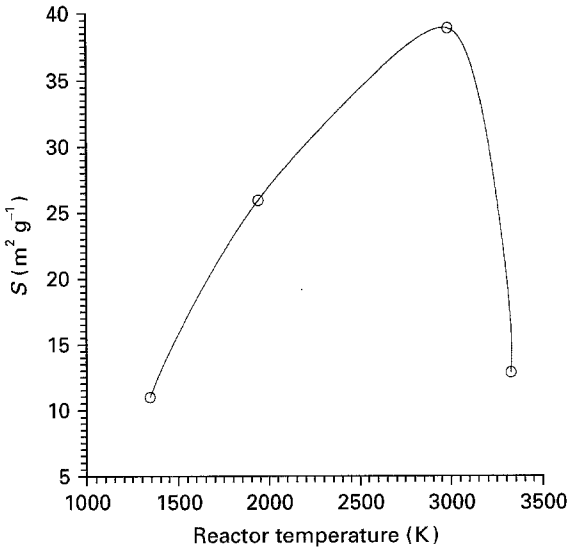

Figure 17 Dependence of the specific surface of the pigments (S) on the average temperature in the PCR (T).

the same time, the pigment's colour changes from black at low temperatures to red-violet at a PCR temperature of 3350 K. Plasma chemical treatment of burnt pyrites is useful when it is necessary to prepare pigments with well developed specific surface.

4. Conclusions

A simplified one-dimensional model describing the motion, heating, melting and evaporation of particles under LTP conditions has been proposed that makes use of substantially fewer physical constants and thermodynamic variables compared with a complex model published earlier [17]. The calculations performed concerning the motion, heating, melting and evaporation of iron particles of < 50 μm size in high enthalpy plasma jets are in good agreement with the results of the complex model, e.g. the values of the particle diameter (radius) as a function of its location along the PCR axis, i.e. the residence time, the particle temperature depending on the residence time (location along the PCR axis), etc. A scheme for the formation of UDP is also proposed.

Further, the conditions for producing iron oxides were investigated with pigment qualification (iron oxide pigments) by oxidation in electric arc LTP of iron dichloride (crystal hydrate), iron sulfate (monohydrate), roughly dispersed iron and burnt pyrites. The impossibility of synthesizing iron oxide through oxidation of iron in LTP at temperatures above 3500 K is proved thermodynamically. Based on X-ray and chemical analysis of the pigments, and on some thermodynamic and kinetic considerations, a plausible mechanism for oxidation in a plasma is proposed.

By selecting suitable plasma-chemical process parameters, one can control the specific surface of iron oxides with pigment qualification within the 5–93 $m^2 g^{-1}$ range. This specific surface is several times higher than that of pigments obtained by known methods; its dependence on the average PCR temperature exhibits a maximum. The chemical content of the pigments (Fe_2O_3 and Fe_3O_4 content, respectively the Fe^{3+}/Fe^{2+} ratio) is an unequivocal function of plasmatron power (the average PCR temperature) when all other process conditions are kept constant. The effect of adding aluminium and aluminium oxide on the pigment properties of the products is a five-fold rise of the specific surface compared with pigments obtained using the same technique in the absence of additivies. In addition, the bulk mass of the pigments diminishes, while their colour range widens. Depending on the plasma-chemical process conditions, the pigment colour varies from black to light brown passing through dark brown, red-brown and red-violet. The pigments possess surface coverage of 2–2.5 $g m^{-2}$ at medium oil absorption and good compatibility with other finely dispersed pigments.

Acknowledgements

The X-ray analysis of the samples was performed in the Technological University of Sofia on a TUR-M62 apparatus by Dr R. Radanov. The electron microscope photographs were made by Dr E. Kashchieva on a Philips EM-301 transmission electron microscope. This work is partially supported by contract No. X563 of the National Research Foundation.

References

1. E. BELENKIY and I. RISKIN, "Himiya i tehnologiya pigmentov" (Himiya, Moskva, Leningrad, 1976) pp 156–60.
2. G. DIEZ and P. NIEDNER, *Masch. und Industriansrüst* **46**(12) (1966) 12.
3. I. RISKIN, *Zh. Prikl. Him.* **12** (1939) 686.
4. A. KAMEL, A. ABDALAH and HY. Ee-BARADIE, *J. Appl. Chem.&Biotechnol.* **22**(12) (1972) 1209.
5. Japanese Patent 49/11 316 (1974).
6. USSR Patent 278 660 (1970).
7. N. SOROKINA, I. BLIYKHER and V. ZAKUTINSKYY, *Tr. Uralskogo nauchno himicheskogo instituta* **25** (1973) 73.
8. US Patent 3 325 252 (1967).
9. British Patent 1 092 883 (1967).
10. US Patent 3 340 007 (1967).
11. *ibid.*, 2 642 339 (1953).
12. *ibid.*, 3 793 444 (1974).
13. USSR Patent 213 773 (1968).
14. USA Patent 3 419 351 (1968).
15. British Patent 1 085 450 (1967).
16. A. LIUTIY, B. MAIMUR, T. ODINTZOVA and I. SCHMELEV, in "Generatori nizkotemperaturnoi plasmi", edited by A. V. Likov (Energiya, Moskva, 1969) p. 413.
17. G. VISSOKOV and L. BRAKALOV, *J. Mater. Sci.* **18** (1983) 2011.
18. G. VISSOKOV, DSc thesis, Sofia (1994) p. 370.
19. A. KLIYATCHKO-GURVITCH, *Izv. USSR. Acad. Sci. OHN* **10** (1961) 1884.
20. S. ROSTOVTZEV, "Teoria metallurgitcheskih protzessov" (Metallurgiya, Moskva, 1956) pp 150–52.

Received 4 July
and accepted 21 December 1995